

Article

Evolution of Precipitates and Microhardness of L-PBF Inconel 625 Through Relevant Thermal Treatment

Tahmina Keya ^{1,*}, Ralf D. Fischer ¹, Mohanish Andurkar ², Scott M. Thompson ³, Valentina O'Donnell ³, John Gahl ³ and Barton C. Prorok ^{1,*}

¹ Department of Materials Engineering, Auburn University, Auburn, AL 36849, USA; rdf0009@auburn.edu

² Alan Levin Department of Mechanical & Nuclear Engineering, Kansas State University, Manhattan, KS 66506, USA; mandurkar@ksu.edu

³ University of Missouri Research Reactor (MURR), University of Missouri, Columbia, MO 65211, USA; smthompson@missouri.edu (S.M.T.); valentina.odonnell@gmail.com (V.O.); gahlj@missouri.edu (J.G.)

* Correspondence: tzk0041@auburn.edu (T.K.); prorocb@auburn.edu (B.C.P.)

Abstract: Laser powder bed fusion (L-PBF) is a metal additive manufacturing (AM) technique that produces a unique microstructure significantly different from wrought microstructure. Inconel 625 (IN625) is an alloy widely used to manufacture complex parts, but it comes with its own unique challenges. The alloy is prone to precipitation under elevated temperatures, which makes designing suitable heat treatment to tailor the desired microstructure and mechanical properties critical. Traditional heat treatment for wrought IN625 cannot be applied to L-PBF IN625; therefore, it is vital to understand the evolution of precipitates on the way to complete recrystallization. This study focuses on these precipitates in IN625 produced by the L-PBF technique. Heat treatments at 700 °C, 900 °C, and 1050 °C were performed separately to encourage the precipitation of strengthening γ'' , the detrimental δ phase, and the dissolution of precipitates, respectively. γ'' precipitates were found in the as-printed condition and at 700 °C. δ precipitates were detected at 700 and 900 °C. Carbides and Al-rich oxides were observed in all conditions of L-PBF IN625. Texture analysis showed grain growth along the build direction with strong (100) texture at temperatures up to 900 °C. Weak and random texture with equiaxed grains was observed at 1050 °C, which is similar to wrought IN625.

Keywords: additive manufacturing; laser powder bed fusion; Ni-based superalloy; microstructure; δ precipitate; γ'' precipitate



Citation: Keya, T.; Fischer, R.D.; Andurkar, M.; Thompson, S.M.; O'Donnell, V.; Gahl, J.; Prorok, B.C. Evolution of Precipitates and Microhardness of L-PBF Inconel 625 Through Relevant Thermal Treatment. *Alloys* **2024**, *3*, 295–312. <https://doi.org/10.3390/alloys3040018>

Academic Editor: Pavel Krakhmalev

Received: 30 October 2024

Revised: 5 December 2024

Accepted: 11 December 2024

Published: 17 December 2024



Copyright: © 2024 by the authors. Licensee MDPI, Basel, Switzerland. This article is an open access article distributed under the terms and conditions of the Creative Commons Attribution (CC BY) license (<https://creativecommons.org/licenses/by/4.0/>).

1. Introduction

Inconel 625 (IN625) is a Ni-based superalloy that derives its superior strength primarily from solid solution strengthening associated with its Nb and Mo constituents. It can also form secondary phases at elevated temperatures, resulting in appreciable precipitation hardening [1,2]. Due to its excellent mechanical properties and corrosion resistance in extreme environments, IN625 is a preferred alloy choice in aerospace, energy, and medical applications [3,4]. Components in these industries often require complex or novel geometry that is challenged by IN625's machinability due to its high strength. Additive manufacturing (AM) techniques are an excellent choice when faced with such circumstances. Laser powder bed fusion (L-PBF) is a metal AM process in which a high-energy laser beam is used to melt layers of metal powder to build a part from a 3D CAD model. L-PBF is a widely used technique for producing IN625 parts [4–6]. The microstructure produced by AM techniques is significantly different from that of traditional manufacturing processes [6–11]. The fast cooling rate during the L-PBF process produces a fine dendritic microstructure with elemental segregation on interdendritic boundaries. Such microstructure greatly influences the precipitation behavior in L-PBF IN625. Precipitation is likely to occur much faster in L-PBF IN625 compared to its wrought counterparts [11–13]. Five major precipitates in

IN625 have been addressed in the literature, namely γ'' , δ , and carbides such as MC, M_6C , and $M_{23}C_6$ [3]. Oxide inclusions have also been mentioned in several studies [10,14,15].

The γ'' phase is the major strengthening precipitate in IN625 [2,16,17]. It has a body-centered tetragonal (BCT) $D0_{22}$ crystal structure with a chemical composition of $Ni_3(Nb, Ti, Al)$ [16,18–21]. Several research groups reported the formation of metastable γ'' precipitate in the range of 550–750 °C [17,19,20,22,23]. These precipitates can be plate, disc, lens, spherical, or elliptical shapes. It can take a long time to form γ'' phase in traditionally manufactured IN625 [19], but precipitation may occur as soon as 1 h in AM-produced materials [9,24]. Amato et al. reported the formation of γ'' precipitate in as-built IN625 produced via selective laser melting [6]. It is a challenging task to be certain about the presence of γ'' with characterization techniques such as scanning electron microscopy (SEM), energy dispersive spectroscopy (EDS), or X-ray diffraction (XRD), especially when the size and amount of the precipitate are small [25]. The XRD peaks of γ matrix and γ'' phase virtually overlap [23]. Therefore, the presence of γ'' precipitate in the as-built condition or short-term heat treatment condition has rarely been presented with convincing proof.

A more studied precipitate that forms in IN625 is the δ phase, which has an orthorhombic $D0_a$ structure with a composition of Ni_3Nb or $Ni_3(Nb, Mo)$ [19,26]. It can have an acicular, plate, or globular shape. Researchers have reported the formation of the δ phase at 650–982 °C [19,20,26,27]. The stable δ phase generally forms from metastable γ'' precipitates when it dissolves into the matrix, leaving a high local concentration of Nb atoms [24,27]. It usually nucleates at grain boundaries (GBs) followed by growth into the grain. δ precipitates form much faster in AM materials compared with wrought IN625 due to Nb and Mo enrichment and Cr deficiency in the interdendritic regions [9,12]. Stoudt et al. reported the formation of δ precipitates in L-PBF IN625 at 870 °C after 15 min [12]. They found δ precipitation in the interdendritic region that grew in number and size with time. Lass et al. reported the formation of plate-shaped δ precipitates at 870 °C for 1 h in L-PBF IN625 [9].

Carbides are also generally found in traditionally and additively manufactured IN625. They have cubic crystal structures with compositions of Nb-rich MC; Ni-, Cr-, and Mo-rich M_6C ; and Cr-rich $M_{23}C_6$ [3,13,19]. These carbides can form in both the matrix and GBs and can contribute to the strengthening of IN625 [2]. They usually appear in blocky, globular, dendritic, or irregular, random shapes. The primary carbide MC is usually transformed into secondary M_6C or $M_{23}C_6$ upon aging heat treatment [3,13]. Carbides can be found in AM-produced IN625 in both as-built as well as heat-treated conditions [9,10,13,24,28,29]. Metallic and non-metallic oxides are also found in AM-produced alloys. These oxide formations are promoted by the oxygen inclusion in the material during the inert gas atomization process and by the presence of moisture/oxygen in the build chamber [14,15,30,31]. Lou et al. reported the presence of Si-rich oxide in L-PBF stainless steel and its detrimental effect on the mechanical properties in a high-temperature water environment [32]. Deng et al. reported the formation and evolution of Si, Mn-rich non-metallic oxides, and Cr-rich metallic oxides in the absence of Si/Mn in L-PBF 316L [31]. Few researchers have mentioned metallic oxide formation in AM as-built and heat-treated IN625 [10,14,15].

Mechanical properties such as hardness are significantly affected by the formation and change in precipitates. The formation of the strengthening phase γ'' causes an appreciable rise in hardness, but over-aging may lead to the coarsening of γ'' and the formation of the detrimental phase δ , which results in reduced hardness. Studies performed on AM IN625 have reported significantly higher hardness compared with traditionally manufactured IN625 [24,33]. The microstructure produced by selective laser melting (SLM) is finer and more textured than forged and laser melting deposition (LMD)-produced microstructures [33]. AM microstructures contribute to superior hardness and strength, but poor ductility compared with wrought material. The heat treatment of AM parts at 1100 °C generates mechanical properties more comparable to those of wrought parts. The superior mechanical properties found in L-PBF IN625 may also be attributed to the high dislocation density along with the fine dendritic microstructure [29].

Although the microstructure of L-PBF as-printed and heat-treated IN625 has been studied by multiple researchers, a more detailed and comprehensive look at each precipitate, confirming their type, is still warranted to better understand the evolution of the microstructure for various applications. Identifying the precipitates in each condition and studying their evolution through relevant heat treatment will aid in tailoring the desired microstructure and hence the mechanical properties of L-PBF IN625, as well as in designing a suitable heat treatment. Traditionally manufactured alloys have been widely studied for different applications, but the post-processing techniques used for such alloys may not be suitable for AM-produced parts [9].

In this study, as-printed IN625 samples were heat-treated in the range of 700–1050 °C to encourage the formation of strengthening γ'' precipitate, the detrimental δ precipitate, and, finally, the dissolution of all precipitates. A detailed electron backscatter diffraction (EBSD) analysis that explains the texture and a unique grain size evolution of all L-PBF samples is presented. Since the evolution of the major precipitates in different heat treatment conditions is the primary concern, the results are organized and discussed separately for each precipitate instead of each heat treatment. The formation of the δ phase at a temperature as low as 700 °C after 2 h is an interesting finding that was established in this study using TEM analysis that cannot be proven otherwise. The presence of carbides and Al_2O_3 is reported in all conditions, and this has not been widely mentioned in the literature, to the best of authors' knowledge. This study also shows that the driving force behind some Al_2O_3 formation is the formation of the δ phase from the γ'' phase. Microhardness has also been measured and compared to observe the effects of heat treatment.

2. Materials and Methods

2.1. Materials and Laser Powder Bed Fusion

Inconel 625 powder was obtained from Concept Laser and possessed the composition given in Table 1. The particle size distribution was determined using the laser diffraction method. The particle diameter distribution is specified by 10%, 50%, and 90% percentiles, according to $Dv(10) = 20.28 \mu\text{m}$, $Dv(50) = 31.31 \mu\text{m}$, and $Dv(90) = 48.4 \mu\text{m}$, with mean particle diameter $\bar{d} = 31.31 \mu\text{m}$. L-PBF cubes of 1 cm \times 1 cm \times 1 cm were printed using a Concept Laser MLab 100R Cusing system manufactured by Concept Laser (Cincinnati, OH, USA), Lichtenfels, Germany. The laser scanning parameters were 90 W of power, 800 mm/s velocity, and a hatch spacing of 60 μm to produce optimum-density samples; further details can be found in prior published work [7,8]. As a comparator to the L-PBF samples, wrought Inconel 625 of AMS5599 specification was procured. Here, 1 cm \times 1 cm \times 0.5 cm cubes were sectioned from a stock plate using wire electrical discharge machining (EDM). The composition of wrought IN625 is also provided in Table 1.

Table 1. Elemental composition of Inconel 625 powder and wrought (% in weight).

% wt.	Ni	Cr	Mo	Fe	Nb + Ta	Co	C	P	S	Al	Ti	Mn
L-PBF	Bal	21	9	<5.0	3.5	<1.0	<0.1	<0.015	<0.015	<0.4	<0.4	<0.5
Wrought	Bal	22.36	9.0	4.72	3.32	0.8	0.035	0.009	0.005	0.08	0.3	0.18

2.2. Heat Treatment

Heat treatments were conducted on L-PBF cubes in a Treet-All Box Furnace (Lindberg, MI, USA) under an inert argon gas atmosphere. The heat treatment conditions are listed in Table 2. Direct aging at three different temperatures—700 °C (γ'' phase formation), 900 °C (δ phase formation), and 1050 °C (solution anneal)—was chosen for 2 h each, separately.

Table 2. Heat treatment parameters.

Sample	Heat Treatment Temperature (°C)	Time (Hours)	Cooling Method
AP	As-printed (No HT)	N/A	N/A
700_2h	700	2	Air Cooled
900_2h	900	2	Air Cooled
1050_2h	1050	2	Air Cooled

Heat treatment schedules (temperatures and times) were determined using time–temperature–transformation (TTT) diagrams for L-PBF and wrought IN625 found in the literature [7,8].

2.3. Metallographic Sample Preparation

Cubes produced via L-PBF were sectioned along their build direction (BD) to reveal the surface perpendicular to sweep direction (SD). The cut surfaces from both L-PBF and wrought IN625 were mounted in CONDUCTOMOUNT™ mounting resin to aid further preparation. Mounted samples were ground and then polished down to 0.25 µm colloidal silica suspension. Additional polishing using a 0.04 µm colloidal silica suspension on a vibratory polisher was performed to facilitate EBSD. For microstructure and precipitation analysis, samples were electro-etched with 70% phosphoric acid at 3–5 volts for 5–40 s.

2.4. Characterization Techniques

Microstructure analysis was performed using various analytical tools, such as scanning electron microscopy (SEM) imaging, transmission electron microscopy (TEM) including selected area electron diffraction (SAED), energy dispersive spectroscopy (EDS), and EBSD for texture analysis. SEM, EDS, and EBSD were performed using a JEOL 7000F SEM unit (JEOL Ltd., Tokyo, Japan). TEM analysis was performed using an FEI Tecnai F20 electron microscope to capture bright field images as well as SAED to identify precipitates. Further details on the equipment and techniques can be found in prior publications by the authors [8].

Vickers hardness was measured to determine and assess the mechanical performance of each sample condition. A LECO DM-400 hardness tester (LECO Corporation, St Joseph, MI, USA) was used to measure microhardness with an applied load of 1000 gf (1 kgf = 9.8 N) for 30 s.

3. Results

3.1. General Microstructure

Figure 1 presents SEM micrographs of the general microstructure of L-PBF as-printed and heat-treated IN625. The microstructure of each L-PBF sample was acquired on the surface, normal to powder SD after etching. “U”-shaped melt pools are clearly visible in as-printed L-PBF IN625, as shown in Figure 1a. The width of these melt pools approximately ranges between 100 and 120 µm, as their exact width is obscured by their overlap. A columnar and cellular structure can be observed that indicates the growth of the dendritic structure in different directions, a phenomenon reported by others [6–8,10,24,33]. Columnar growth along the BD through several layers can be observed as well. Melt pool boundaries are still visible after heat treatment at 700 °C for 2 h (Figure 1b). Remnants of melt pools can be seen in the 900_2h sample in Figure 1c. Here, some regions recrystallized, and precipitates grew at the prior interdendritic regions at this temperature. These precipitates will be identified and discussed in detail in later sections. The melt pool boundaries, precipitates, and dendritic structure with elemental segregation are completely dissolved in the 1050_2h sample (Figure 1d). The microstructure of this sample consists of equiaxed grains. This microstructure is comparable to the wrought microstructure that was shown in previous work [8].

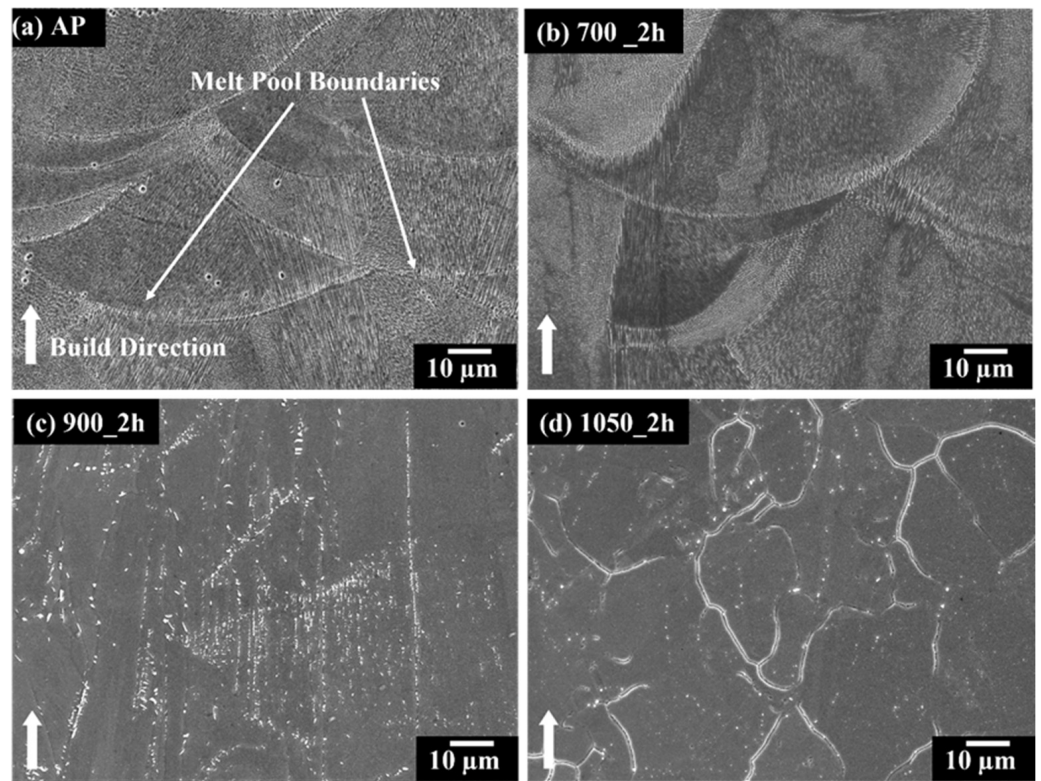


Figure 1. SEM images of the microstructure of L-PBF IN625; (a) as-printed, (b) heat-treated at 700 °C for 2 h, (c) heat-treated at 900 °C for 2 h, and (d) heat-treated at 1050 °C for 2 h.

Figures 2 and 3 reveal the texture evolution in L-PBF samples compared to wrought IN625. The inverse pole figures (IPFs) along the BD (IPF-BD) in Figure 2 show that there are large, elongated grains growing roughly along the BD and a reasonable number of very small grains that are $\leq 30 \mu\text{m}$ in the AP, 700_2h, and 900_2h samples. These observations are in agreement with the findings of other researchers for IN625 [10,34]. A $\text{BD} \parallel \langle 100 \rangle$ texture can also be observed in as-printed L-PBF IN625 (Figure 2a) that becomes stronger after heat treatment at 700 °C (Figure 2b) and 900 °C (Figure 2c) before the texture becomes random in the 1050_2h sample (Figure 2d), which is similar to the texture of its wrought counterpart (Figure 2e). The pole figures (PFs) in Figure 3 convey a similar message where the texture appears to become stronger along the (100) plane with increasing heat treatment temperature. The multiple uniform density (MUD) values in the PFs are kept in the same range to facilitate visual comparison between different planes as well as for different samples. The average grain size of the AP sample is $40.4 \pm 16.8 \mu\text{m}$, which increases to $52.1 \pm 19.7 \mu\text{m}$ after heat-treating at 900 °C, as shown in Figure 2f. A noticeable change is observed in the 1050_2h sample in which the grains become equiaxed with a random texture, as shown in Figures 2d and 3d, and it becomes similar to that of the wrought sample shown in Figures 2e and 3e. The grain size here is reduced to $20.43 \pm 9.26 \mu\text{m}$ at this temperature, which is still double the grain size of wrought IN625.

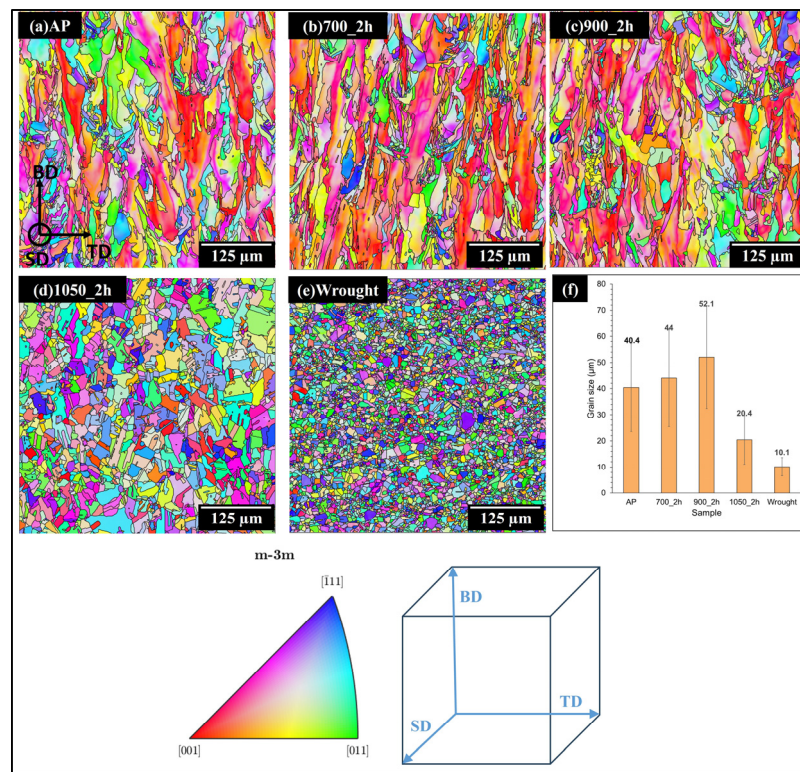


Figure 2. (a–e) Inverse pole figure (IPF) maps of as-printed and heat-treated L-PBF IN625 along the BD compared to wrought IN625; (f) grain size evolution of each sample.

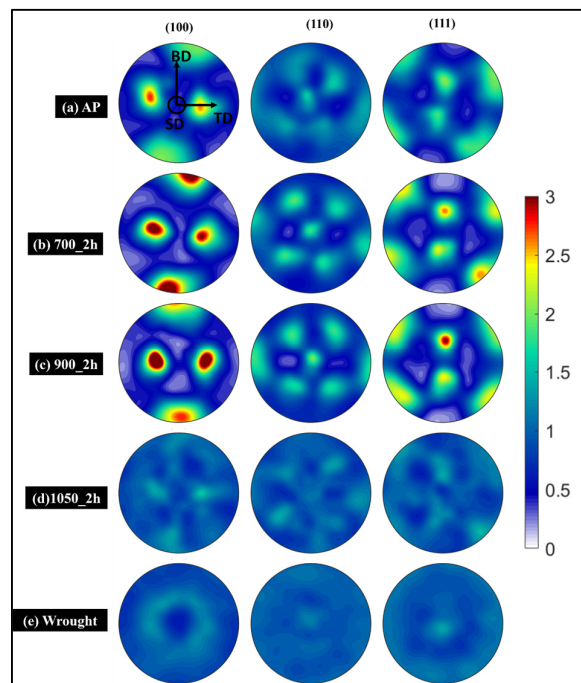


Figure 3. Pole figures (PFs) of as-printed and heat-treated L-PBF IN625 compared to wrought IN625.

3.2. Formation of γ'' Precipitate

The γ'' precipitate was only observed in the AP and 700_2h samples. Figure 4 shows bright-field TEM micrographs with SAED from the AP and 700_2h conditions. For the AP condition, the bright-field image in Figure 4a shows disc-shaped precipitates on the order

$$[100]_{\delta} \parallel \langle 110 \rangle_{\gamma}$$

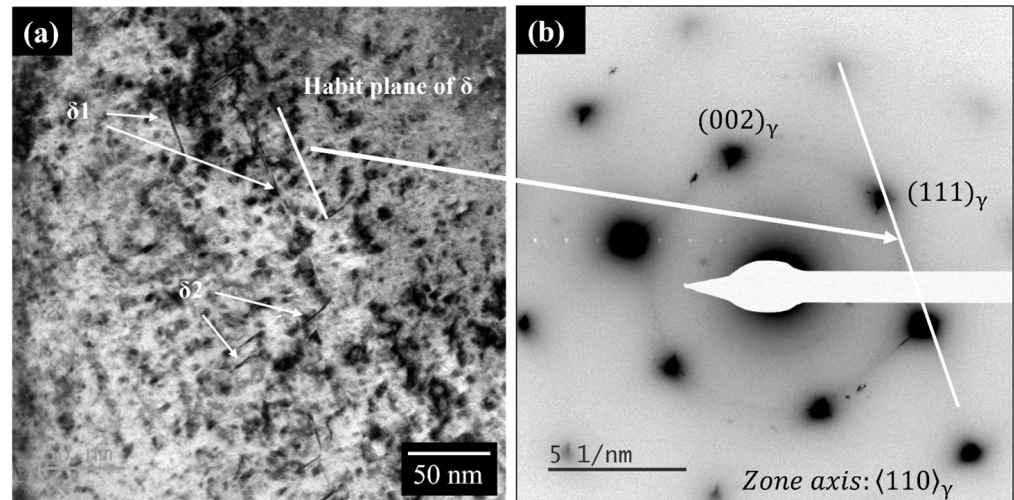


Figure 5. (a) TEM image inside a grain in the 700_2h sample; (b) SAED pattern from (a) indicating the presence of δ .

With slight rotation of the sample, the precipitates disappear, which indicates that they are actually plate-shaped and not needle-shaped. Although the heat treatment temperature is in the range that favors the formation of δ precipitate in IN625, to the best knowledge of the authors, it has not been reported before for L-PBF IN625 for a temperature as low as 700 °C and a treatment time as low as 2 h. The δ precipitate is actually formed from the metastable γ'' phase [19], which is already present in the as-printed and 700_2h conditions. Thus, the presence of γ'' precipitate likely facilitated the early formation of the δ phase.

Figure 6 shows the TEM images and electron diffraction patterns of the δ precipitate in the 900_2h condition. An overall view of the sample is shown in Figure 6a, where needle-like and plate-shaped precipitates can be observed both within grains and at GBs. The size of these precipitates ranges from a few hundred nm to over 1 μm depending on their location. Thick plate-shaped precipitates on GBs were identified as δ phase by SAED pattern, as shown in Figure 6b,c. The smaller precipitates within the grains are also identified as δ precipitates, as shown in Figure 6d–g. Therefore, the precipitates are actually two-dimensional plate-shaped forms that are rotated at a certain angle, giving a one-dimensional appearance. One such precipitate is shown in Figure 6d. The high-resolution TEM (HRTEM) images are presented in Figure 6e,f. Here, the coherency between the δ precipitate and the γ matrix can be observed. Three areas in the HRTEMs were chosen to perform fast Fourier transform (FFT) simulations, defined as 1 and 2 in Figure 6e and 3 in Figure 6f. In area 1, the majority of the area contains only the γ matrix, as identified from the simulation. Area 2 also primarily covers the γ matrix. However, the FFT simulation reveals the presence of a stacking fault, likely caused by the formation of the δ precipitate. Area 3 includes both parts of the precipitate as well as the γ matrix. Here, the FFT simulation presented in Figure 6g confirms it as a δ precipitate within the grain. The precipitates inside the grain appeared to grow approximately 10 times larger at 900 °C compared with those at 700 °C. By contrast, the δ precipitates formed on the GB appear to be around a few hundred nanometers to over 1 μm , significantly larger than those inside the grain.

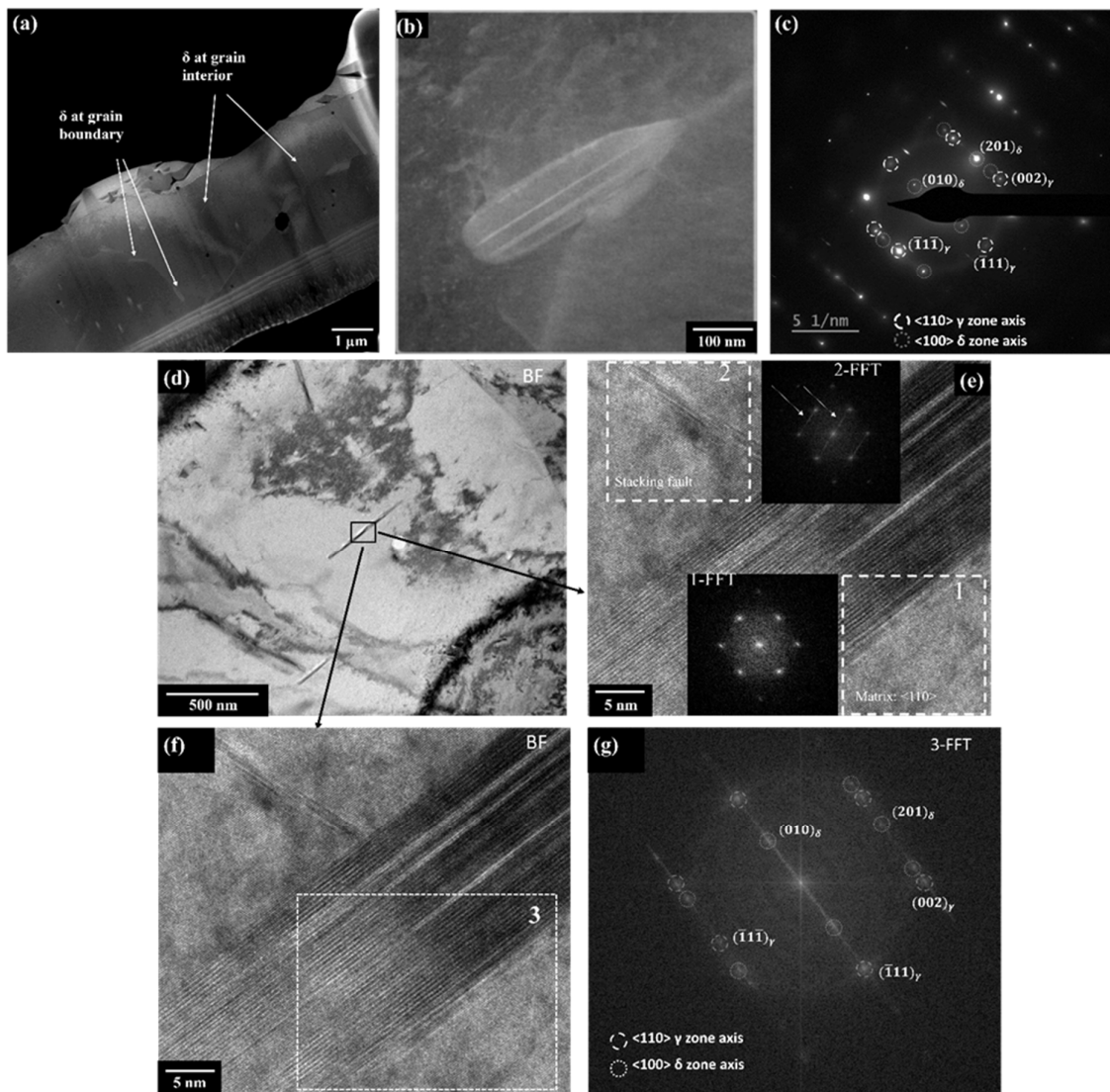


Figure 6. (a) TEM thin film taken from the 900_2h sample; (b) bright-field TEM image of a δ precipitate on GB and (c) corresponding SAED pattern; (d) bright-field TEM image of a δ precipitate inside the grain; (e) HRTEM image of a δ precipitate with FFT showing γ matrix and stacking fault; (f) HRTEM image of a δ precipitate with (g) an FFT pattern of area 3 indexed for the δ precipitate.

3.4. Formation of Carbides

Carbides are another precipitate typically observed in alloy IN625 [1,2,19]. In this work, they were observed in all L-PBF samples, as shown in Figure 7. EDS line scans (indicated by yellow arrows) was performed on each sample to confirm the presence of carbides. Clusters of irregularly shaped carbides were observed in locations where two melt pool boundaries met in AP IN625 (Figure 7a). The deficiency of Ni and Cr, coupled with Nb and Mo enrichment in the particles, indicated the presence of (Nb, Mo)C. The irregular morphology, formation during solidification, and interdendritic location also point toward the formation of MC [2,19,29]. The formation of carbides is generally facilitated by Nb and Mo segregation in the interdendritic region due to a fast cooling rate [29]. The accurate size of the carbides is challenging to measure since they can be overlapped with the elemental segregation, but it appeared to be in the range of around 500–900 nm. Marchese et al. reported the presence of nanometric-sized Nb-rich MC near the interdendritic region of as-built L-PBF IN625. Liu et al. [28] observed circular $M_{23}C_6$ precipitation in as-built IN625 produced via SLM as well as laser-engineered net shaping (LENS) in the intergranular region.

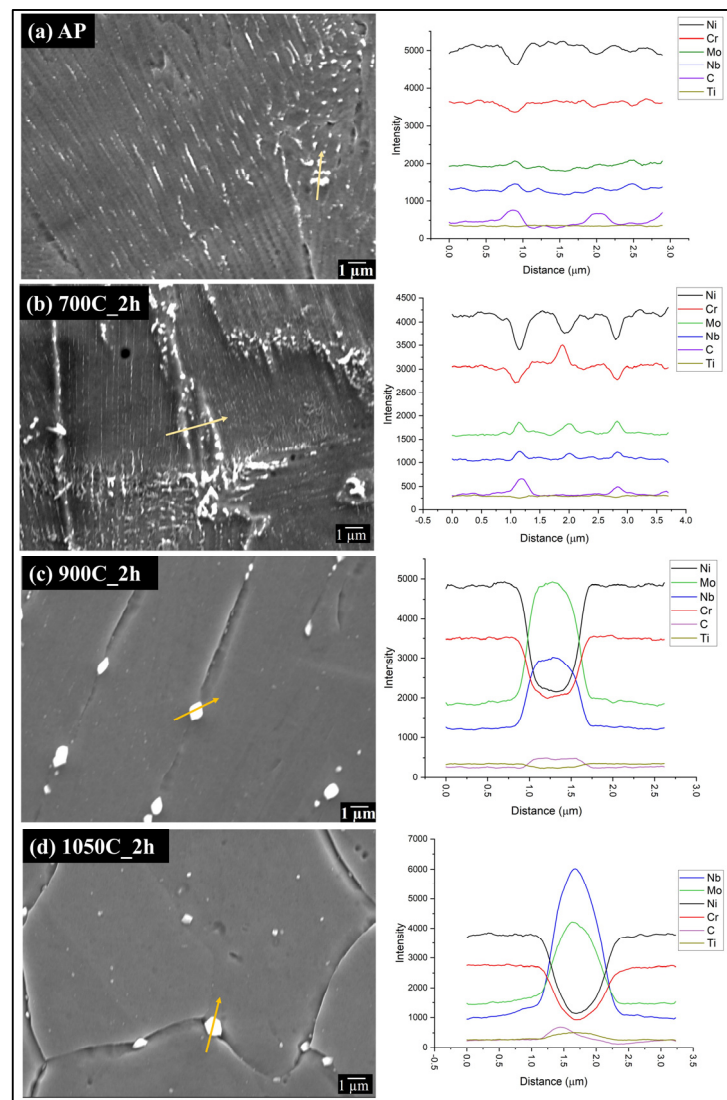


Figure 7. Carbides with corresponding EDS patterns in (a) AP, (b) 700_2h, (c) 900_2h, and (d) 1050_2h samples.

For the 700 °C treatment, similar carbides of a similar size as those in the as-printed condition are also found on the GBs, as shown in Figure 7b and the corresponding EDS pattern. These carbides are also rich in Nb and Mo and deficient in Ni and Cr. Their irregular shapes indicate that they are most likely the primary MC carbides that formed during printing. The heat treatment temperature is also not high enough for these carbides to evolve or to form any other type of carbide. $M_{23}C_6$ has been shown to form at similar temperatures; however, they are usually rather rich in Cr [2,3,19].

Block-shaped carbides are observed in evanescent interdendritic regions of the 900_2h sample, as shown in Figure 7c. Considering the treatment temperature and their composition as measured by EDS, they appear to be the already-formed primary MC carbide that grew after aging. The carbides are around 770 nm. However, some significantly smaller carbides on the order of 300 nm can also be observed in the matrix. These carbides are likely secondary carbides and are developed in the form of Nb- and Mo-rich MC and M_6C at this temperature [3,19]. The presence of 9% Mo in the alloy composition also facilitates the formation of Mo-rich M_6C [2].

Carbides can be found in both intergranular as well as intragranular locations in the 1050_2h sample (see Figure 7d). Larger carbides mostly reside on GBs with a size of 380–970 nm. Smaller carbides can be found on both GBs as well as grain interiors with a size

range of 160–305 nm. Also, a few large carbides with a size of approximately 600–700 nm can be found inside the grains [8]. The larger carbides are primary MC carbides that grew upon aging. The smaller carbides may have been transformed from primary carbides in the form of either MC or M_6C . The presence of carbides around this temperature has been widely reported for both traditional and AM IN625 [2,10,13,19,24].

3.5. Formation of Al_2O_3 Particles

Al_2O_3 particles were found in all L-PBF samples in this work. Figure 8a represents a TEM bright-field image of the AP sample along with its corresponding EDS spectrum of the precipitate, indicated by yellow arrow. It is clear from the EDS analysis that the particle is rich in Al and O while being deficient in Ni, Cr, Nb, and Mo. The size of the precipitates is approximately 35–95 nm. They are observed everywhere in the sample, including at the GBs as well as grain interiors. The presence of metallic oxide inclusions in as-printed L-PBF IN625 has been well described by Staroń et al. [14]. According to the literature, oxide inclusions are likely caused by the presence of oxygen in powder as well as in the build chamber environment [10,14,15].

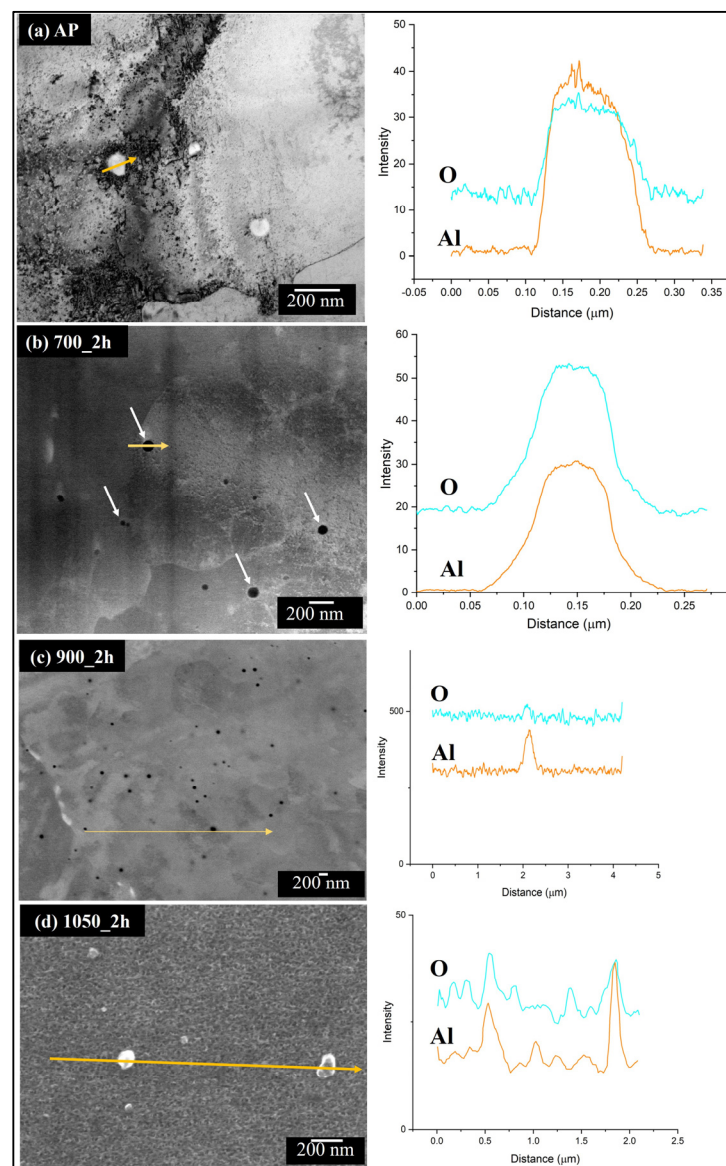


Figure 8. Al_2O_3 particles with EDS spectra in (a) TEM BF image from AP; (b) TEM BSE image from 700_2h; (c) SEM BSE image from 900_2h; and (d) SEM image from the 1050_2h sample.

The observed oxides showed little change with heat treatment. Figure 8b shows a TEM backscatter electron image (BSE) of the 700_2h sample. These oxides, indicated by white arrows, also appear evenly dispersed throughout the sample with a similar size distribution as the AP sample. Increasing the treatment temperature to 900 °C (Figure 8c) shows no obvious change in size to the existing Al_2O_3 precipitates. As described above, this temperature corresponds to the significant formation of the δ precipitate phase. An interesting observation is the emergence of new, small Al_2O_3 precipitates adjacent to the δ precipitates, as shown in Figure 9. The white dashed box shows a magnified view of the δ precipitate on which EDS analysis was performed. Based on their location, it can be inferred that some of these Al-rich oxides may have formed during the conversion of existing γ'' precipitates, which contain Al, into Al-free δ precipitates [19]. After treatment to 1050 °C, Al_2O_3 particles continued to be observed throughout the sample (see Figure 8d). These precipitates evolved in size to increase the upper range to approximately 160 nm in diameter, similar to what has been observed by others [10,14,15].

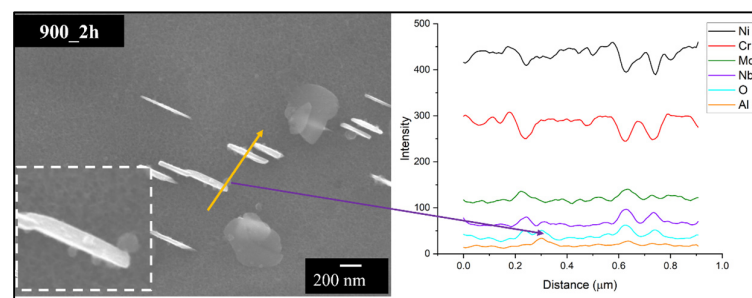


Figure 9. Al_2O_3 particles on and around δ precipitates.

3.6. Microhardness

The variations in microstructure and precipitation with direct aging in this work showed a significant change in microhardness behavior. Figure 10 shows the evolution of microhardness with heat treatment of L-PBF IN625 at increasing temperature compared with a wrought IN625 counterpart prepared by aerospace material specification AMS 5599 [39]. The hardness of AP IN625 was $341.5 \pm 6.06 \text{ HV}_{1.0}$, which was the highest measured of all samples and significantly higher than the wrought sample of $223.25 \pm 2.86 \text{ HV}_{1.0}$. Hardness then reduced somewhat to $324.75 \pm 4.49 \text{ HV}_{1.0}$ after heat treatment at 700 °C for 2 h. The hardness further decreased to $284.5 \pm 12.66 \text{ HV}_{1.0}$ upon heat treatment at 900 °C. The lowest hardness values were achieved in the 1050 °C heat treatment, where the hardness reduced to $222.5 \pm 5.17 \text{ HV}_{1.0}$, nearly equivalent to the hardness of wrought IN625.

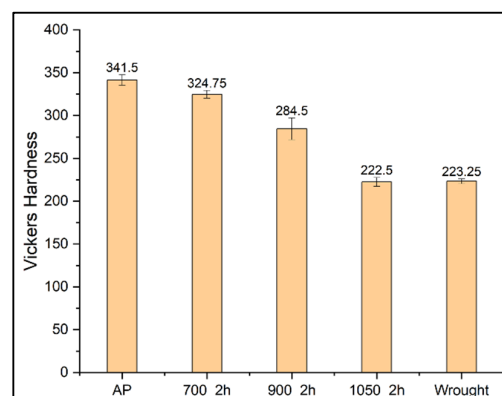


Figure 10. Microhardness on L-PBF heat-treated IN625 compared to wrought IN625.

4. Discussion

The U-shape melt pools in the L-PBF AP sample shown in Figure 1a are caused by the Gaussian energy distribution of the laser beam interaction with the alloy [24]. An overlapping melt pool structure enables high part density with no gap between the melt pool boundaries [8,24]. Columnar growth along the BD resulted from the re-melting of layers combined with directional solidification along the BD. Elongated grains in different directions are formed during printing due to rapid cooling and directional solidification [40,41]. The equiaxed grain structure with the presence of annealing twins in the L-PBF 1050_2h sample shown in Figures 1d and 2d indicates residual stress release [10,29].

The IPFs in Figure 2 reveal the evolution of grain size in L-PBF IN625. A combination of large and small grains is present in AP, 700_2h, and 900_2h. Li et al. suggested that the sizes of the smaller grains are induced by the remelting near the melt pool boundaries and epitaxial growth of the grains [24]. Heat treatment at 1050 °C makes the microstructure similar to that of wrought IN625; however, there is a rather significant difference in the grain size. As shown in Figure 2f, the grain size of L-PBF 1050_2h is double that of wrought IN625. L-PBF is a near-net shape production technique, and the microstructure or grain size is typically not altered using mechanical processes after manufacturing a part. Therefore, suitable thermal processes need to be designed to achieve comparable microstructure and mechanical properties to those of its traditional counterparts.

The increase in grain size from the AP condition to the 700_2h and 900_2h conditions is attributed to the thermal coarsening due to annealing. However, an unexpected drop in grain size is observed in the 1050_2h sample. Although precipitates, elemental segregation, melt pool boundaries, and dendritic structure are dissolved at this temperature, the counteracting effect of recrystallization caused this reduction in grain size. This sudden drop in grain size at 1050 °C can be explained by Figure 11 which also provides the kernel average misorientation plots for all L-PBF samples. It can be observed that there is a dominance of misorientations inside the grain for the AP, 700_2h, and 900_2h samples since there are groups of dendrites that are slightly misoriented with each other. With heat treatment at 1050 °C, those groups of dendrites make their own grains, causing the larger grains to break apart into smaller grains and almost complete recrystallization. It is interesting to observe that the KAM plot of wrought IN625 shows the presence of misorientation, hence the strain in the commercially available material that was induced via thermo-mechanical processes to obtain the desired mechanical properties. This detailed analysis of the texture and the grain structure using EBSD is unique to this study, which will help other researchers interpret the microstructural analysis of L-PBF IN625 correctly.

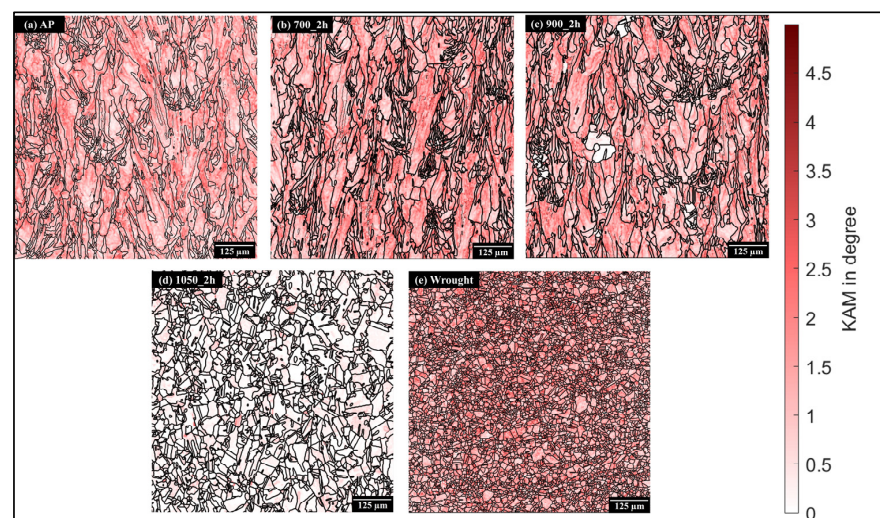


Figure 11. Kernel average misorientation for L-PBF and wrought IN625 samples.

The γ'' precipitate phase is the main strengthening precipitate that is found in several Ni-based superalloys [16,42–45]. It has a body-centered tetragonal crystal structure that is coherent with the FCC γ matrix. The strengthening they impart results from coherency strain hardening [2,16]. These precipitates have an ellipsoidal disc shape that is induced by the lattice misfit with the γ matrix. The [001] axis or c-axis of the tetragonal γ'' precipitate is longer than the c-axis of the FCC γ matrix, causing a large misfit strain that encourages the disc-like shape of the γ'' precipitate [16,46]. An interesting observation regarding the L-PBF AP sample was the absence of the [001] γ'' variant. According to Oblak et al., the [001] γ'' variant can be suppressed upon direct aging under compressive stress [16]. In the case of L-PBF fabrication, it can be linked to the ultrafast cooling rate and directional solidification that caused residual stress in the finished part [8,10,24]. Amato et al. reported the presence of γ'' precipitate in L-PBF IN625 with diffraction patterns [6], and it was later cited by many authors; however, there is a lack of further evidence and more discussion on the evolution of the variants of this precipitate in L-PBF IN625. To compare the γ'' precipitation in L-PBF IN625 to its wrought counterpart, the strengthening phase is not readily found in commercially available IN625 that has not been precipitation-hardened. To perform precipitation hardening on traditional IN625 at 700 °C, almost 8 h of heat treatment is required, according to the available TTT diagrams [19]. It has been established by researchers that precipitation occurs faster in additively manufactured IN625 [12].

The [001] γ'' variant appeared in the diffraction pattern taken from the 700_2h sample shown in Figure 4d. This is due to the release of the tensile residual stress that had developed from L-PBF processing. The tensile stress in AP IN625 was measured to be 77 ± 15 MPa, as reported in prior work by the authors [47]. Direct aging under tensile residual stress mimicked the effect of stress aging under tensile load, which promoted the growth of the [001] γ'' variant [16,35,46,48]. The size of the other two variants was unchanged since stress aging under tensile load suppresses the growth of [100] γ'' and [010] γ'' compared to [001] γ'' [16]. It is worth mentioning that although the appearance of the [001] γ'' variant proves some stress release in the 700_2h sample, it is not significant enough to be captured by the KAM plot shown in Figure 11b. The stress release is not very visible in Figure 11b since the KAM plot is dominated by dendritic misorientations in the grains.

The presence of the γ'' phase in the AP state explains its relatively high hardness, as presented in Figure 10. This high hardness is not only attributed to the fine dendritic microstructure resulting from L-PBF's ultra-fast cooling rate and elemental segregation, as described in the literature [24,49], but also due in part to the formation of the γ'' strengthening phase. In the 700_2h sample, additional γ'' precipitates formed and grew with heat treatment. In addition, the formation of a modest amount of δ precipitate was observed upon the dissolution of some γ'' . Although 700 °C is within the range of δ phase formation, due to its very small size and amount, it is challenging to determine its presence. TEM images along with the diffraction pattern from a specific direction presented in Figure 5 was the only successful way to confirm δ phase formation at a temperature as low as 700 °C after only 2 h of heat treatment, which has not been proven before, to the authors' best knowledge. Despite the formation of additional precipitates, that hardness reduction is attributed to the slight increase in grain size, as shown in Figure 2f. In the 900_2h sample, although the δ precipitates formed on a wide scale, it generally formed from the dissolution of the existing γ'' strengthening precipitates. Despite its contribution in part as a strengthening mechanism, it was accompanied by a significant increase in grain size that dominated hardness behavior. Similar to the case of γ'' precipitation, the δ phase is also not found in wrought IN625 without further heat treatment. To encourage δ phase formation in traditional IN625 at 900 °C, almost 40 h of heat treatment is necessary [19]. Therefore, a stress relief annealing treatment at a temperature close to 900 °C for 1 h can be performed on wrought IN625 without risking the detrimental δ precipitation [2].

The hardness of the 1050_2h sample decreased despite a significant reduction in grain size. This is attributed to the dissolution of major precipitates, dendritic structure, and stress

release through recrystallization and grain growth of an equiaxed microstructure. Although the hardness is very similar between the 1050 °C and wrought samples, the average grain size of the wrought samples is approximately half that of the 1050 °C samples. Also, the KAM plot in Figure 11 indicates the presence of misorientation and hence strain in wrought IN625 as opposed to L-PBF 1050_2h. This indicates that direct solution annealing of L-PBF samples generates microstructures that retain some aspects of their as-printed forms, such as precipitates, which results in higher hardness. The position of the carbides in the microstructure also plays a role. The carbides are distributed in both the GBs and the grain interior in the L-PBF 1050_2h sample, whereas they are found mainly on GBs in wrought IN625. This phenomenon is discussed in detail in [8].

5. Conclusions

The microstructure of L-PBF IN625 with the evolution of each precipitate upon heat treatment was discussed in this study. Strengthening the γ'' phase, detrimental δ phase, carbides, and aluminum oxide particles were found in different conditions. The findings can be summarized as follows:

- Melt pool boundaries along with dendritic microstructure growing in different directions were observed on the plane normal to sweep direction in as-printed L-PBF IN625. The microstructure stayed fairly similar at 700 °C. Partial recrystallization took place at 900 °C with disappearing melt pool boundaries. The microstructure was almost fully recrystallized with a dissolved dendritic structure and precipitates at 1050 °C.
- Large, elongated grains growing along the build direction were observed in the as-printed, 700 °C, and 900 °C states of L-PBF IN625. The texture became stronger along the (100) plane with increasing heat treatment temperature until it became random and weak at 1050 °C. The microstructure of L-PBF IN625 at 1050 °C is similar to wrought IN625; however, the grain size is still fairly large compared to that in the wrought condition.
- Metastable γ'' precipitates form during the manufacturing stage, causing higher hardness in as-printed L-PBF IN625. Two out of three variants of the precipitate were detected in the TEM SAED pattern. The third variant appeared at 700 °C, which was caused by direct aging of AP IN625 that contained residual stress.
- Stable δ phase formed at 700 °C upon the dissolution of some γ'' precipitates, causing lower hardness compared with AP. Two variants of δ precipitate were observed at 700 °C, which grew upon heat treatment at 900 °C. The formation and growth of δ precipitate caused a stacking fault in the primary γ matrix. The hardness kept decreasing at 900 °C as well due to the recrystallization and dissolution of the γ'' phase.
- Carbides were found for all conditions of L-PBF IN625. Considering the EDS patterns and morphology of the particles, they appear to be MC carbides rich in Nb and Mo.
- Metallic oxides rich in Al were also found in all L-PBF samples. The presence of oxygen in feedstock powder and build chamber may cause these oxide inclusions. However, some of the Al_2O_3 particles surrounding δ precipitates may be caused by the dissolution of Al-containing γ'' precipitates.

Studying the microstructure and mechanical properties of L-PBF Inconel 625 is essential to understanding how the rapid cooling and localized heating inherent in the process affect its unique microstructure, including grain size, phase distribution, and precipitate formation. These microstructural characteristics directly influence the material's mechanical properties, such as hardness, strength, ductility, fatigue, and corrosion resistance, which are critical for its performance in demanding industries like aerospace and energy. In certain cases, understanding the microstructure can help analyze the material's performance during application without immediate post-application analysis such as post-irradiation behavior [50]. Additionally, it can contribute to establishing TTT diagrams for AM IN625. Such studies will help optimize the post-processing of L-PBF parts to achieve desired properties, reduce defects, and ensure reliability, making the material suitable for high-performance applications.

Author Contributions: Conceptualization, B.C.P.; methodology, T.K., and R.D.F.; software, T.K.; validation, T.K.; formal analysis, T.K.; investigation, T.K.; resources, M.A. and S.M.T.; data curation, T.K., M.A., and V.O.; writing—original draft preparation, T.K.; writing—review and editing, R.D.F., V.O., S.M.T. and B.C.P.; visualization, T.K.; supervision, S.M.T., J.G., and B.C.P.; project administration, S.M.T., J.G., and B.C.P.; funding acquisition, S.M.T., J.G., and B.C.P. All authors have read and agreed to the published version of the manuscript.

Funding: The U.S. Department of Energy’s Office of Nuclear Energy, award number DE-NE0008865.

Data Availability Statement: Data are included in the article. Further information is available upon request.

Acknowledgments: The authors gratefully acknowledge the research support provided by the staff of the Alabama Materials Institute, Tuscaloosa, AL, USA.

Conflicts of Interest: The authors declare no conflicts of interest.

References

1. Shoemaker, L.E. Alloys 625 and 725: Trends in Properties and Applications. In *Proceedings of the Superalloys 718, 625, 706 and Various Derivatives (2005)*; TMS: Pittsburg, PA, USA, 2005; pp. 409–418.
2. Donachie, M.J.; Donachie, S.J. *Superalloys: A Technical Guide*, 2nd ed.; ASM International: Detroit, MI, USA, 2002; ISBN 978-1-62708-267-9.
3. Liu, X.; Fan, J.; Zhang, P.; Cao, K.; Wang, Z.; Chen, F.; Liu, D.; Tang, B.; Kou, H.; Li, J. Influence of Heat Treatment on Inconel 625 Superalloy Sheet: Carbides, γ'' , δ Phase Precipitation and Tensile Deformation Behavior. *J. Alloys Compd.* **2023**, *930*, 167522. [[CrossRef](#)]
4. Gola, K.; Dubiel, B.; Kalembe-Rec, I. Microstructural Changes in Inconel 625 Alloy Fabricated by Laser-Based Powder Bed Fusion Process and Subjected to High-Temperature Annealing. *J. Mater. Eng. Perform.* **2020**, *29*, 1528–1534. [[CrossRef](#)]
5. Gonzalez, J.A.; Mireles, J.; Stafford, S.W.; Perez, M.A.; Terrazas, C.A.; Wicker, R.B. Characterization of Inconel 625 Fabricated Using Powder-Bed-Based Additive Manufacturing Technologies. *J. Mater. Process. Technol.* **2019**, *264*, 200–210. [[CrossRef](#)]
6. Amato, K. Comparison of Microstructures and Properties for a Ni-Base Superalloy (Alloy 625) Fabricated by Electron Beam Melting. *J. Mater. Sci. Res.* **2012**, *1*, 3. [[CrossRef](#)]
7. Keya, T.; O'Donnell, V.; Lieben, J.; Romans, A.; Harvill, G.; Andurkar, M.; Gahl, J.; Thompson, S.M.; Prorok, B.C. Effects of Heat Treatment and Fast Neutron Irradiation on the Microstructure and Microhardness of Inconel 625 Fabricated via Laser-Powder Bed Fusion. In *Proceedings of the 2021 International Solid Freeform Fabrication Symposium*, Austin, TX, USA, 2–4 August 2021.
8. Keya, T.; Bikmukhametov, I.; Shmatok, A.; Harvill, G.; Brewer, L.N.; Thompson, G.B.; Andurkar, M.; Thompson, S.M.; O'Donnell, V.; Prorok, B.C. Evolution of Microstructure and Its Influence on the Mechanical Behavior of LPBF Inconel 625 upon Direct Aging. *Manuf. Lett.* **2023**, *35*, 732–742. [[CrossRef](#)]
9. Lass, E.A.; Stoudt, M.R.; Williams, M.E.; Katz, M.B.; Levine, L.E.; Phan, T.Q.; Gnaeupel-Herold, T.H.; Ng, D.S. Formation of the Ni₃Nb δ -Phase in Stress-Relieved Inconel 625 Produced via Laser Powder-Bed Fusion Additive Manufacturing. *Metall. Mater. Trans. A* **2017**, *48*, 5547–5558. [[CrossRef](#)]
10. Li, C.; White, R.; Fang, X.Y.; Weaver, M.; Guo, Y.B. Microstructure Evolution Characteristics of Inconel 625 Alloy from Selective Laser Melting to Heat Treatment. *Mater. Sci. Eng. A* **2017**, *705*, 20–31. [[CrossRef](#)]
11. Zhang, F.; Levine, L.E.; Allen, A.J.; Stoudt, M.R.; Lindwall, G.; Lass, E.A.; Williams, M.E.; Idell, Y.; Campbell, C.E. Effect of Heat Treatment on the Microstructural Evolution of a Nickel-Based Superalloy Additively-Manufactured by Laser Powder Bed Fusion. *Acta Mater.* **2018**, *152*, 200–214. [[CrossRef](#)]
12. Stoudt, M.R.; Lass, E.A.; Ng, D.S.; Williams, M.E.; Zhang, F.; Campbell, C.E.; Lindwall, G.; Levine, L.E. The Influence of Annealing Temperature and Time on the Formation of δ -Phase in Additively-Manufactured Inconel 625. *Metall. Mater. Trans. A* **2018**, *49*, 3028–3037. [[CrossRef](#)]
13. Keller, T.; Lindwall, G.; Ghosh, S.; Ma, L.; Lane, B.M.; Zhang, F.; Kattner, U.R.; Lass, E.A.; Heigel, J.C.; Idell, Y.; et al. Application of Finite Element, Phase-Field, and CALPHAD-Based Methods to Additive Manufacturing of Ni-Based Superalloys. *Acta Mater.* **2017**, *139*, 244–253. [[CrossRef](#)]
14. Staroń, S.; Dubiel, B.; Gola, K.; Kalembe-Rec, I.; Gajewska, M.; Pasiowiec, H.; Wróbel, R.; Leinenbach, C. Quantitative Microstructural Characterization of Precipitates and Oxide Inclusions in Inconel 625 Superalloy Additively Manufactured by L-PBF Method. *Metall. Mater. Trans. A* **2022**, *53*, 2459–2479. [[CrossRef](#)]
15. Son, K.; Kassner, M.E.; Lee, K.A. The Creep Behavior of Additively Manufactured Inconel 625. *Adv. Eng. Mater.* **2020**, *22*, 1900543. [[CrossRef](#)]
16. Oblak, J.M.; Paulonis, D.F.; Duvall, D.S. Coherency Strengthening in Ni Base Alloys Hardened by D₂₂ γ' Precipitates. *Metall. Trans.* **1974**, *5*, 143–153. [[CrossRef](#)]
17. Sundararaman, M.; Mukhopadhyay, P.; Banerjee, S. Precipitation of the δ -Ni₃Nb Phase in Two Nickel Base Superalloys. *Metall. Trans. A* **1988**, *19*, 453–465. [[CrossRef](#)]
18. Yu, L.-J.; Marquis, E.A. Precipitation Behavior of Alloy 625 and Alloy 625 Plus. *J. Alloys Compd.* **2019**, *811*, 151916. [[CrossRef](#)]

19. Floreen, S.; Fuchs, G.E.; Yang, W.J. The Metallurgy of Alloy 625. *Superalloys* **1994**, *718*, 13–37.
20. Suave, L.M.; Cormier, J.; Villechaise, P.; Soula, A.; Hervier, Z.; Bertheau, D.; Laigo, J. Microstructural Evolutions during Thermal Aging of Alloy 625: Impact of Temperature and Forming Process. *Metall. Mater. Trans. A* **2014**, *45*, 2963–2982. [[CrossRef](#)]
21. Kirman, I.; Warrington, D.H. The Precipitation of Ni₃Nb Phases in a Ni-Fe-Cr-Nb Alloy. *Metall. Trans.* **1970**, *1*, 2667–2675. [[CrossRef](#)]
22. Rai, S.K.; Kumar, A.; Shankar, V.; Jayakumar, T.; Rao, K.B.S.; Raj, B. Characterization of Microstructures in Inconel 625 Using X-Ray Diffraction Peak Broadening and Lattice Parameter Measurements. *Scr. Mater.* **2004**, *51*, 59–63. [[CrossRef](#)]
23. Sarkar, A.; Mukherjee, P.; Barat, P.; Jayakumar, T.; Mahadevan, S.; Rai, S.K. Lattice Misfit Measurement in Inconel 625 by X-Ray Diffraction Technique. *Int. J. Mod. Phys. B* **2008**, *22*, 3977–3985. [[CrossRef](#)]
24. Li, S.; Wei, Q.; Shi, Y.; Zhu, Z.; Zhang, D. Microstructure Characteristics of Inconel 625 Superalloy Manufactured by Selective Laser Melting. *J. Mater. Sci. Technol.* **2015**, *31*, 946–952. [[CrossRef](#)]
25. Dinda, G.P.; Dasgupta, A.K.; Mazumder, J. Laser Aided Direct Metal Deposition of Inconel 625 Superalloy: Microstructural Evolution and Thermal Stability. *Mater. Sci. Eng. A* **2009**, *509*, 98–104. [[CrossRef](#)]
26. Shankar, V.; Rao, K.B.S.; Mannan, S.L. Microstructure and Mechanical Properties of Inconel 625 Superalloy. *J. Nucl. Mater.* **2001**, *288*, 222–232. [[CrossRef](#)]
27. Baldan, R.; Silva, A.A.A.P.d.; Tanno, T.M.; da Costa, E.T.; Brentegani, J.V.N.; Couto, A.A. Experimental Investigation of Delta Phase Precipitation in Inconel 625 Superalloy Aged at 550, 625 and 725 °C. *Mater. Res.* **2020**, *23*, e20190546. [[CrossRef](#)]
28. Chen, F.; Wang, Q.; Zhang, C.; Huang, Z.; Jia, M.; Shen, Q. Microstructures and Mechanical Behaviors of Additive Manufactured Inconel 625 Alloys via Selective Laser Melting and Laser Engineered Net Shaping. *J. Alloys Compd.* **2022**, *917*, 165572. [[CrossRef](#)]
29. Marchese, G.; Lorusso, M.; Parizia, S.; Bassini, E.; Lee, J.-W.; Calignano, F.; Manfredi, D.; Terner, M.; Hong, H.-U.; Ugues, D. Influence of Heat Treatments on Microstructure Evolution and Mechanical Properties of Inconel 625 Processed by Laser Powder Bed Fusion. *Mater. Sci. Eng. A* **2018**, *729*, 64–75. [[CrossRef](#)]
30. Deng, P.; Song, M.; Yang, J.; Pan, Q.; McAllister, S.; Li, L.; Prorok, B.C.; Lou, X. On the Thermal Coarsening and Transformation of Nanoscale Oxide Inclusions in 316L Stainless Steel Manufactured by Laser Powder Bed Fusion and Its Influence on Impact Toughness. *Mater. Sci. Eng. A* **2022**, *835*, 142690. [[CrossRef](#)]
31. Deng, P.; Karadge, M.; Rebak, R.B.; Gupta, V.K.; Prorok, B.C.; Lou, X. The Origin and Formation of Oxygen Inclusions in Austenitic Stainless Steels Manufactured by Laser Powder Bed Fusion. *Addit. Manuf.* **2020**, *35*, 101334. [[CrossRef](#)]
32. Lou, X.; Andresen, P.L.; Rebak, R.B. Oxide Inclusions in Laser Additive Manufactured Stainless Steel and Their Effects on Impact Toughness and Stress Corrosion Cracking Behavior. *J. Nucl. Mater.* **2018**, *499*, 182–190. [[CrossRef](#)]
33. Nguejio, J.; Szymtka, F.; Hallais, S.; Tanguy, A.; Nardone, S.; Martinez, M.G. Comparison of Microstructure Features and Mechanical Properties for Additive Manufactured and Wrought Nickel Alloys 625. *Mater. Sci. Eng. A* **2019**, *764*, 138214. [[CrossRef](#)]
34. Marchese, G.; Bassini, E.; Parizia, S.; Manfredi, D.; Ugues, D.; Lombardi, M.; Fino, P.; Biamino, S. Role of the Chemical Homogenization on the Microstructural and Mechanical Evolution of Prolonged Heat-Treated Laser Powder Bed Fused Inconel 625. *Mater. Sci. Eng. A* **2020**, *796*, 140007. [[CrossRef](#)]
35. Qin, H.; Bi, Z.; Yu, H.; Feng, G.; Zhang, R.; Guo, X.; Chi, H.; Du, J.; Zhang, J. Assessment of the Stress-Oriented Precipitation Hardening Designed by Interior Residual Stress during Ageing in IN718 Superalloy. *Mater. Sci. Eng. A* **2018**, *728*, 183–195. [[CrossRef](#)]
36. Rong, Y.; Chen, S.; Hu, G.; Gao, M.; Wei, R.P. Prediction and Characterization of Variant Electron Diffraction Patterns for γ'' and δ Precipitates in an Inconel 718 Alloy. *Metall. Mater. Trans. A Phys. Metall. Mater. Sci.* **1999**, *30*, 2297–2303. [[CrossRef](#)]
37. Dehmas, M.; Lacaze, J.; Niang, A.; Viguier, B. TEM Study of High-Temperature Precipitation of Delta Phase in Inconel 718 Alloy. *Adv. Mater. Sci. Eng.* **2011**, *2011*, 940634. [[CrossRef](#)]
38. Zhang, J.P.; Ye, H.Q.; Kuo, K.H.; Amelinckx, S. A High-Resolution Electron Microscopy Study of the Domain Structure in Ni₃Nb. II. Orientation and General Domains. *Phys. Status Solidi (a)* **1986**, *93*, 457–462. [[CrossRef](#)]
39. SAE MOBILUS. Available online: <https://saemobilus.sae.org/content/ams5599> (accessed on 4 September 2023).
40. Wang, Z.; Guan, K.; Gao, M.; Li, X.; Chen, X.; Zeng, X. The Microstructure and Mechanical Properties of Deposited-IN718 by Selective Laser Melting. *J. Alloys Compd.* **2012**, *513*, 518–523. [[CrossRef](#)]
41. Calandri, M.; Yin, S.; Aldwell, B.; Calignano, F.; Lupoi, R.; Ugues, D. Texture and Microstructural Features at Different Length Scales in Inconel 718 Produced by Selective Laser Melting. *Materials* **2019**, *12*, 1293. [[CrossRef](#)]
42. Kulawik, K.; Buffat, P.A.; Kruk, A.; Wusatowska-Sarneck, A.M.; Czyrska-Filemonowicz, A. Imaging and Characterization of γ' and γ'' Nanoparticles in Inconel 718 by EDX Elemental Mapping and FIB-SEM Tomography. *Mater. Charact.* **2015**, *100*, 74–80. [[CrossRef](#)]
43. Zhang, R.Y.; Qin, H.L.; Bi, Z.N.; Tang, Y.T.; Araújo de Oliveira, J.; Lee, T.L.; Panwisawas, C.; Zhang, S.Y.; Zhang, J.; Li, J.; et al. γ'' Variant-Sensitive Deformation Behaviour of Inconel 718 Superalloy. *J. Mater. Sci. Technol.* **2022**, *126*, 169–181. [[CrossRef](#)]
44. Zhang, H.; Li, C.; Guo, Q.; Ma, Z.; Li, H.; Liu, Y. Improving Creep Resistance of Nickel-Based Superalloy Inconel 718 by Tailoring Gamma Double Prime Variants. *Scr. Mater.* **2019**, *164*, 66–70. [[CrossRef](#)]
45. Cao, G.H.; Sun, T.Y.; Wang, C.H.; Li, X.; Liu, M.; Zhang, Z.X.; Hu, P.F.; Russell, A.M.; Schneider, R.; Gerthsen, D.; et al. Investigations of γ' , γ'' and δ Precipitates in Heat-Treated Inconel 718 Alloy Fabricated by Selective Laser Melting. *Mater. Charact.* **2018**, *136*, 398–406. [[CrossRef](#)]

46. Zhang, R.Y.; Qin, H.L.; Bi, Z.N.; Li, J.; Paul, S.; Lee, T.L.; Zhang, S.Y.; Zhang, J.; Dong, H.B. Evolution of Lattice Spacing of Gamma Double Prime Precipitates During Aging of Polycrystalline Ni-Base Superalloys: An In Situ Investigation. *Metall. Mater. Trans. A* **2020**, *51*, 574–585. [[CrossRef](#)]
47. Andurkar, M.; Suzuki, T.; Omori, M.; Prorok, B.; Gahl, J. Residual Stress Measurements via X-Ray Diffraction Cos α Method on Various Heat-Treated Inconel 625 Specimens Fabricated via Laser-Powder Bed Fusion. In Proceedings of the 2021 International Solid Freeform Fabrication Symposium, Austin, TX, USA, 2–4 August 2021.
48. Zhang, R.; Qin, H.; Bi, Z.; Li, J.; Paul, S.; Lee, T.; Nenchev, B.; Zhang, J.; Kabra, S.; Kelleher, J.; et al. Using Variant Selection to Facilitate Accurate Fitting of γ'' Peaks in Neutron Diffraction. *Metall. Mater. Trans. A* **2019**, *50*, 5421–5432. [[CrossRef](#)]
49. Tian, Z.; Zhang, C.; Wang, D.; Liu, W.; Fang, X.; Wellmann, D.; Zhao, Y.; Tian, Y. A Review on Laser Powder Bed Fusion of Inconel 625 Nickel-Based Alloy. *Appl. Sci.* **2020**, *10*, 81. [[CrossRef](#)]
50. Andurkar, M.; O'Donnell, V.; Keya, T.; Prorok, B.C.; Gahl, J.; Thompson, S.M. Fast Neutron Irradiation-Induced Hardening in Inconel 625 and Inconel 718 Fabricated via Laser Powder Bed Fusion. *Prog. Addit. Manuf.* **2024**. [[CrossRef](#)]

Disclaimer/Publisher's Note: The statements, opinions and data contained in all publications are solely those of the individual author(s) and contributor(s) and not of MDPI and/or the editor(s). MDPI and/or the editor(s) disclaim responsibility for any injury to people or property resulting from any ideas, methods, instructions or products referred to in the content.